X-ray diffraction from Si/Ge layers: Diffuse scattering in the region of total external reflection

J.-P. Schlomka,* M. Tolan, L. Schwalowsky,† O. H. Seeck, J. Stettner, and W. Press
Institut für Experimentalphysik, Christian-Albrechts-Universität Kiel,
Olshausenstrasse 40-60, 24098 Kiel, Germany
(Received 14 September 1994)

In this paper it is shown that diffuse-scattering experiments within the region of total external reflection can be explained quantitatively using the distorted-wave Born approximation for layer systems. Three Si/Ge samples with different degrees of complexity were investigated. The simultaneous analysis of the specular reflected intensity and the diffuse scattering leads to one consistent set of interface and layer parameters, which is able to fit both the shapes and the locations of all dynamic peaks in the off-specular scans and the characteristics of the reflected intensity. Therefore the distorted-wave Born approximation seems to give a correct and complete description of the diffuse scattering in the region of total external reflection.

I. INTRODUCTION

For small incident angles, x-ray diffraction becomes surface sensitive and an optical treatment is possible (for a review see, e.g., Ref. 1). The real part of the refractive index is slightly smaller than one which leads to the phenomenon of total external reflection.[2] In this region the penetration depth of the incoming waves is rather small and the scattered intensities contain mainly information about the structures in the near surface region. Whereas x-ray reflectivity has become a common tool for investigating density profiles of thin films and multilayers in a nondestructive manner,[3–8] many works now concentrate on the quantitative analysis of the diffusely scattered intensity. In contrast to the specularly reflected x-ray beam, which contains information averaged over the illuminated area of the sample, the nonspecularly diffuse intensity is sensitive to the lateral structure of rough interfaces, in particular to the respective height-height correlation functions.

Theoretically the specularly as well as the diffusely scattered intensity can be calculated within the first-order Born approximation (kinematic theory). This approach can explain several experiments quantitatively for incidence angles that are large compared to the critical angle.[9–15] For small incidence angles, in the region of the critical angle multiple-scattering effects cannot be neglected and the simple Born approximation breaks down.

Sinha *et al.*[16] have calculated the diffuse scattering cross section within the so-called distorted-wave Born approximation[17] (DWBA) for a single surface that is valid for small incidence angles. Later this result was confirmed by Pynn.[18] De Boer[19,20] has shown that an inclusion of second-order effects into the theory avoids the principal problem of the DWBA, namely, the conseravation of the total scattered intensity.[21] Recently Holý *et al.*[22,23] have worked out the DWBA for layer systems including the effect of vertical correlations between the interfaces. Such correlations are of decisive importance for many systems because in most thin-film preparation techniques [e.g., sputtering, evaporation, and molecular-beam epitaxy (MBE)] an imperfection of one layer is transferred to the layers above.[9,10,13]

Whereas the scattering theory has been worked out in great detail within the past few years (see also Refs. 24–26), only a few papers with experimental tests of the dynamic calculations have been published up to now.[23,27] Holý and Baumbach have applied their theory to measurements on an AlAs/GaAs multilayer consisting of 20 periods and achieved agreement: Yoneda peaks[16,28] at the positions of the critical angles, Bragg-like peaks caused by the one-dimensional periodicity perpendicular to the surface, and resonantly diffuse scattering peaks due to correlations of the interfaces were well explained by fits. But the shape of these peaks cannot be reproduced by the theory. Therefore the question arises whether these discrepancies are caused by the DWBA itself, which means that the theory is incomplete,[23] or whether these discrepancies have other sources, e.g., the complexity of the samples.

In this paper we show diffuse scattering experiments from three simple systems with increasing complexity: (i) one layer of Ge, (ii) a two-layer system Si/Ge, and (iii) a three-layer system Ge/Si/Ge. All layers were evaporated on Si substrates. The experiments were compared with calculations using the theory of Holý and Baumbach.[23]

The present paper is structured as follows. After the Introduction, the scattering theory (DWBA for correlated layer systems) is briefly presented. Then a description of the samples, the experimental setup, and the scattering geometry follows. After that the special data analysis procedure, the measurements, and the fit results are shown. Conclusions and an outlook finish this paper.

II. THEORY

A. Specular reflectivity

Due to the fact that the calculation of the specularly reflected x-ray intensity is well known for layer systems, only a brief description follows. We assume a sample consisting of N layers $j=1,\ldots,N$. The refractive index n_j of layer j is $n_j=1-\delta_j+i\beta_j$ with the dispersion δ_j and

the absorption β_j. The Fresnel-reflection and -transmission coefficients for each (smooth) interface are $r_{j,j+1}=(k_{z,j}-k_{z,j+1})/(k_{z,j}+k_{z,j+1})$ and $t_{j,j+1}=2k_{z,j}/(k_{z,j}+k_{z,j+1})$, respectively.[29] Here $k_{z,j}$ is the z component (throughout this paper the z axis is directed perpendicular to the surface) of the wave vector in medium j, which is determined by the law of refraction: $k_{z,j}=k_i(n_j^2-\cos^2\alpha_i)^{1/2}$. The glancing angle of incidence is α_i and $k_i=k_f=2\pi/\lambda=k_1$ denotes the modulus of the incoming wave vector (λ is the x-ray wavelength).

The ratio X_j of the amplitudes R_j and T_j of the outgoing to the incoming electromagnetic waves in layer j, which lies between the positions z_{j+1} and z_j (layer thickness $d_j=z_{j+1}-z_j$), can be calculated with the recurrence relation[3,29]

$$X_j=\frac{R_j}{T_j}=e^{-2ik_{z,j}z_j}\frac{r_{j,j+1}+X_{j+1}e^{2ik_{z,j+1}z_j}}{1+r_{j,j+1}X_{j+1}e^{2ik_{z,j+1}z_j}} . \quad (1)$$

If a semi-infinite substrate is assumed, $R_{N+1}=0$ follows and the reflected intensity I can be obtained with Eq. (1) via $I=|R_1|^2$. The amplitude of the incoming x-ray wave was set to $T_1=1$.

Small roughnesses ($\sigma<25$ Å) of layers can be included into the description if the Fresnel reflectivities $r_{j,j+1}$ for smooth interfaces are replaced in Eq. (1) by the coefficients $\tilde{r}_{j,j+1}$ for rough interfaces. An analytical solution for the tanh refractive index profile between layer j and $j+1$

$$n(z)=\frac{n_j+n_{j+1}}{2}-\frac{n_j-n_{j+1}}{2}\tanh\left[\frac{z-z_j}{\sigma_j}\left[\frac{2}{\pi}\right]^{1/2}\right] \quad (2)$$

can be found and leads to the expression[5,6,24]

$$\tilde{r}_{j,j+1}=\frac{\sinh[(\pi/2)^{1.5}\sigma_j(k_{z,j}-k_{z,j+1})]}{\sinh[(\pi/2)^{1.5}\sigma_j(k_{z,j}+k_{z,j+1})]}\times G(\sigma_j,k_{z,j},k_{z,j+1}) .$$

The factor $G(\sigma_j,k_{z,j},k_{z,j+1})$ can be set to one in the case of hard x rays and roughnesses up to $\sigma_j\approx 100$ Å.[30] The tanh profile [Eq. (2)] is very similar to an error-function profile with a Gaussian probability density and root-mean-square (rms) roughness σ_j.[27]

B. Diffuse scattering

An analysis of reflectivity data yields the layer thicknesses d_j and the rms roughnesses σ_j of the system, i.e., averaged information in the direction perpendicular to the surface (but see also the paper of de Boer[19]). Lateral information can only be obtained by an analysis of the diffusely (nonspecularly) scattered intensity, which is caused by lateral inhomogeneities and contains detailed information about the morphology of the interfaces of a layer system.

Whereas in principle the calculation of the reflected intensity is exact [solution of the Helmholz equation with the Parrat formalism, Eq. (1)], the diffusely scattered intensity can only be calculated using various kinds of approximations. In the case of hard x rays and glancing angles of incidence and exit α_i and α_f, respectively, the formulation of the DWBA was first applied to the calculation of the diffuse scattering cross section by Sinha *et al.*[16] and recently extended by Holý *et al.*[22,23] to layer systems. Within this first-order perturbation theory independent eigenstates for the incoming $|\Psi_i\rangle$ and for the outgoing waves $|\Psi_f\rangle$ of a system with flat interfaces are assumed. These eigenstates can easily be calculated for a layer system using Eq. (1) and the additional recurrences for $j=1$ (vacuum) to $j=N+1$ (bulk):

$$R_{j+1}=\frac{1}{t_{j+1,j}}\{T_j r_{j+1,j}e^{-i(k_{z,j+1}+k_{z,j})z_j}+R_j e^{-i(k_{z,j+1}-k_{z,j})z_j}\} ,$$

$$T_{j+1}=\frac{1}{t_{j+1,j}}\{T_j e^{i(k_{z,j+1}-k_{z,j})z_j}+R_j r_{j+1,j}e^{i(k_{z,j+1}+k_{z,j})z_j}\} .$$

Then the eigenstates are

$$|\Psi_i(\mathbf{r})\rangle=T_i(z)e^{i\mathbf{k}_i(z)\cdot\mathbf{r}}+R_i(z)e^{i\mathbf{k}_i'(z)\cdot\mathbf{r}} ,$$

$$|\tilde{\Psi}_f(\mathbf{r})\rangle=T_f^*(z)e^{i\mathbf{k}_f^*(z)\cdot\mathbf{r}}+R_f^*(z)e^{i\mathbf{k}_f'^*(z)\cdot\mathbf{r}} ,$$

introducing a "time-reversed" state $|\tilde{\Psi}_f(\mathbf{r})\rangle$ and the wave vectors $\mathbf{k}_i(z),\mathbf{k}_i'(z)$ and $\mathbf{k}_f(z),\mathbf{k}_f'(z)$ of the incident and scattered waves, respectively. The asterisk denotes a complex conjugate quantity.

To find a solution for the Helmholtz equation $(\Delta+k_i^2)|\Psi\rangle=V(\mathbf{r})|\Psi\rangle$, with $V(\mathbf{r})=k_i^2[1-n^2(\mathbf{r})]$, the potential $V(\mathbf{r})$ is split into a part $V_0(z)$ describing the system with smooth layers and a small perturbation $\delta V(\mathbf{r})$ (i.e., $|q_z\sigma|^2\ll 1$) due to the rough interfaces. The roughness is now leading to a nonzero probability for a transition from state $|\Psi_i\rangle$ to $|\Psi_f\rangle$ with $\mathbf{k}_i\neq\mathbf{k}_f$, which means that the (interface) roughness causes all nonspecular scattering contributions.

A calculation of the transition matrix elements within the DWBA (Ref. 31) finally leads to the following expression for the cross section of the diffuse scattering:[22,23,32]

$$\left[\frac{d\sigma}{d\Omega}\right]_{\text{diff}}=\frac{\mathcal{G}k_1^2}{16\pi^2}\sum_{j,k=1}^{N}(n_j^2-n_{j+1}^2)(n_k^2-n_{k+1}^2)^*\mathcal{C}_{jk}(q_r)\sum_{m,n=0}^{3}\tilde{G}_j^{\,m}\tilde{G}_k^{\,n*}\exp\{-\tfrac{1}{2}[(q_{z,j}^m\sigma_j)^2+(q_{z,k}^{n*}\sigma_k)^2]\}$$

$$=\frac{\mathcal{G}k_1^2}{16\pi^2}\left|\sum_{j=1}^{N}|n_j^2-n_{j+1}^2|^2\mathcal{C}_j(q_r)|(\tilde{G}_j^{\,0}+\tilde{G}_j^{\,3})\exp[-\tfrac{1}{2}(\sigma_j q_{z,j}^0)^2]+(\tilde{G}_j^{\,1}+\tilde{G}_j^{\,2})\exp[-\tfrac{1}{2}(\sigma_j q_{z,j}^1)^2]|^2\right.$$

$$\left.+\sum_{\substack{j,k=1\\ j\neq k}}^{N}(n_j^2-n_{j+1}^2)(n_k^2-n_{k+1}^2)^*\mathcal{C}_{jk}(q_r)\sum_{m,n=0}^{3}\tilde{G}_j^{\,m}\tilde{G}_k^{\,n*}\exp\{-\tfrac{1}{2}[(q_{z,j}^m\sigma_j)^2+(q_{z,k}^{n*}\sigma_k)^2]\}\right| . \quad (3)$$

TABLE I. Two possible analytic continuations of the fields and their respective momentum transfers [see Eq. (3)]. Case I was chosen in the papers of Holý *et al.* (Refs. 22 and 23) and leads to the result of Sinha *et al.* (Ref. 16) for a single interface.

I		II	
$G_j^0=T_{i;j+1}T_{f;j+1}$	$\mathbf{q}_j^0=\mathbf{k}_{i;j+1}+\mathbf{k}_{f;j+1}$	$G_j^0=T_{i;j}T_{f;j}$	$\mathbf{q}_j^0=\mathbf{k}_{i;j}+\mathbf{k}_{f;j}$
$G_j^1=T_{i;j+1}R_{f;j+1}$	$\mathbf{q}_j^1=\mathbf{k}_{i;j+1}-\mathbf{k}_{f;j+1}$	$G_j^1=T_{i;j}R_{f;j}$	$\mathbf{q}_j^1=\mathbf{k}_{i;j}-\mathbf{k}_{f;j}$
$G_j^2=R_{i;j+1}T_{f;j+1}$	$\mathbf{q}_j^2=-\mathbf{q}_j^1$	$G_j^2=R_{i;j}T_{f;j}$	$\mathbf{q}_j^2=-\mathbf{q}_j^1$
$G_j^3=R_{i;j+1}R_{f;j+1}$	$\mathbf{q}_j^3=-\mathbf{q}_j^0$	$G_j^3=R_{i;j}R_{f;j}$	$\mathbf{q}_j^3=-\mathbf{q}_j^0$

Note that a Gaussian probability density of all roughness distributions was assumed to obtain this result. The illuminated area of the sample is denoted by $\mathcal{S}$, $\mathbf{q}_j^m=(\mathbf{q}_r,q_{z,j}^m)^T$ is the momentum transfer within each layer (see Table I), and $\mathcal{C}_j(q_r)$ and $\mathcal{C}_{jk}(q_r)$ are the Fourier transforms of the autocorrelation and cross-correlation functions of the interfaces (see Sec. II C). Furthermore, the factors $\tilde{G}_j^m$ are defined by $\tilde{G}_j^m=G_j^m\exp(-iq_{z,j}^m z_j)$ with the respective expressions for G_j^m given in Table I. Due to different analytic continuations of the wave functions at the interfaces, four different expressions for G_j^m are possible. But only the two in Table I fulfill the condition that the formula for the differential cross section [Eq. (3)] has to be invariant against an exchange of the position of the x-ray source and the detector, i.e., an exchange of $\mathbf{k}_i$ and $\mathbf{k}_f$.

The correlation functions contain the information about the morphology of the surface. To analyze x-ray diffraction data particular correlation functions for the interfaces and correlations between different layers have to be assumed.

C. Correlation functions

The shape of the interface j at the position $z_j(\mathbf{R})=z_j+\phi_j(\mathbf{R})$ can be statistically described via the so-called height-height correlation function $C_j(\mathbf{R})$, which is defined by

$$C_j(\mathbf{R})=\langle\phi_j(\mathbf{r})\phi_j(\mathbf{r}+\mathbf{R})\rangle_{\mathbf{r}} .$$

Here $\mathbf{R}=(x,y)^T$ and $\mathbf{r}$ are vectors within the surface and $\langle\ \rangle_{\mathbf{r}}$ means the average over the (x,y) plane. The (single-valued) function $\phi_j(\mathbf{R})$ is the height fluctuation of the interface z_j at a lateral position $\mathbf{R}$ with roughness $\sigma_j=\sqrt{C_j(0)}$ and vanishing mean value $\langle\phi_j(\mathbf{r})\rangle_{\mathbf{r}}$.

For many isotropic solid surfaces $C_j(\mathbf{R})$ can be represented by the correlation function of a self-affine fractal surface[16]

$$C_j(R)=\sigma_j^2 e^{-(R/\xi_j)^{2h_j}} , \tag{4}$$

with the cutoff (correlation) length ξ_j and the Hurst parameter h_j of the respective interface.[33–35] The quantity ξ_j describes the lateral length scale on which the interface begins to look rough: For $R<\xi_j$ the surface is self-affine rough, whereas for $R>\xi_j$ the surface looks smooth. The Hurst parameter h_j is restricted to the region $0<h_j\leq 1$ (Ref. 36) and defines the fractal box dimension $D_j=3-h_j$ of the interface.[33] Small values of h_j produce extremely jagged surfaces, while values close to one lead to interfaces with smooth hills and valleys. For clarity, Fig. 1 shows possible real structures that are calculated assuming the correlation function given by Eq. (4) with different ξ_j and h_j values, respectively.[35,37] The correlation function defined by Eq. (4) is assumed for all interfaces in the present work. A detailed discussion of other correlation functions is given by Palasantzas.[38,39]

An x-ray scattering experiment does not yield $C_j(\mathbf{R})$ directly, but the respective Fourier transform [see Eq. (3)]

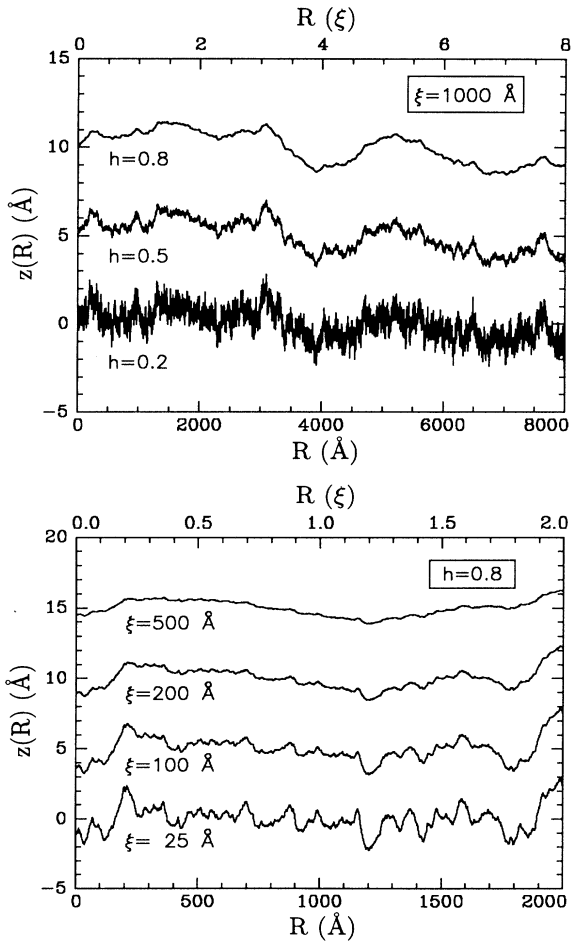

FIG. 1. Calculations of possible one-dimensional surface structures using the correlation function given by Eq.(4) for various values of the parameters ξ and h. A rms roughness of $\sigma=1$ Å was always assumed.

$$\mathcal{C}_j(\mathbf{q}_r)=\frac{1}{2\pi}\int\int_{-\infty}^{+\infty} C_j(\mathbf{R})e^{-i\mathbf{q}_r\cdot\mathbf{R}}d\mathbf{R}\ ,$$

called power spectral density (PSD).[40] For the correlations between different layers j and k, which are important for MBE-grown samples[41] and evaporated films as well, a correlation function

$$C_{jk}(\mathbf{R})=\langle\phi_j(\mathbf{r})\phi_k(\mathbf{r}+\mathbf{R})\rangle_{\mathbf{r}}$$

has to be assumed too.[9,42] In this work the following particular form for the correlations of the roughnesses between the interfaces at the positions z_j and z_k is chosen:

$$C_{jk}(R)=\frac{1}{2}\left[\frac{\sigma_k}{\sigma_j}C_j(R)+\frac{\sigma_j}{\sigma_k}C_k(R)\right]e^{-|z_j-z_k|/\xi_{\perp,jk}}\ , \tag{5}$$

with the correlation functions $C_j(R)$ defined by Eq. (4).[43] The length $\xi_{\perp,jk}$ is the vertical distance over which the correlations between layers j and k are damped by a factor of $1/e$. No correlations are present in the case $\xi_{\perp,jk}=0$ and nearly perfect correlation means that $\xi_{\perp,jk}$ is much larger than the layer thicknesses. In this work, for all vertical correlation lengths $\xi_{\perp,jk}$ the same value $\xi_\perp$ was assumed.

In Eq. (3), $\mathcal{C}_{jk}(q_r)$ denotes the Fourier transform of the correlation function $C_{jk}(R)$. The first sum in Eq. (3) is responsible for the diffuse scattering contributions of the single rough interfaces [$\propto\mathcal{C}_j(q_r)$] and the source of the second sum over j and k with $j\neq k$ are the correlations of these roughnesses [$\propto\mathcal{C}_{jk}(q_r)$].

III. SAMPLES

Three samples with increasing degree of complexity were investigated. In all cases Ge or Si layers were evaporated on Si(100) substrates (provided by Wacker-Chemitronic Burghausen, Germany) using a commercial setup (Balzers BAK 550). Due to the preparation temperatures, amorphous layers are expected. It turns out that these layers typically have densities of about 90–95 % compared to that of bulk single crystals.[44] The film thicknesses of the evaporated layers were controlled by the frequency shift of a quartz thickness monitor. This method is rather inaccurate and allows only coarse estimates. The analysis of the x-ray data, on the other hand, yields very accurate numbers (see Sec. V B). Because the measurements did not take place under vacuum conditions, thin oxide layers between the substrate and the evaporated layers and on top of the samples cannot be avoided.

The nominal parameters of the three samples are as follows. Sample $S1$ consists of one Ge layer of 350 Å thickness evaporated on top of the Si substrate. Sample $S2$ is a two-layer system with 350-Å Ge and 250-Å Si on top of bulk silicon. Finally, sample $S3$ is the three-layer system Ge/Si/Ge on top of Si with the layer thicknesses of 350, 250, and 150 Å, respectively.

IV. EXPERIMENTAL SETUP AND SCATTERING GEOMETRY

A. Setup

The x-ray experiments were performed using a 12-kW rotating anode generator (Rigaku Ru 200) with a copper target and a three-crystal diffractometer (TCD).[45] The x rays from the copper target were collimated by a first slit. Then a Ge(111) monochromator selects the characteristic Cu $K\alpha$ lines from the spectrum. A second slit picks out only the Cu $K\alpha_1$ line with a wavelength of $\lambda=1.54056$ Å, which impinges onto the sample. The sample is mounted on a two-circle goniometer. The accuracy of the step motors, which control the incidence angle α_i and the scattering angle $\Phi=\alpha_i+\alpha_f$, is 0.001°. The detector unit contains a Ge(111) analyzer and a third slit in front of a NaI(Tl) (Canberra) scintillation counter. Vacuum tubes as well as lead shields around the system were installed to increase intensity and to reduce background radiation (for details see Ref. 45). The resolution in the region of the critical angle within the scattering plane of the given TCD is $\delta_{q_x}\approx 5\times10^{-4}$ Å^{-1} and $\delta_{q_z}\approx 7\times10^{-4}$ Å^{-1} parallel and perpendicular to the surface, respectively. The detector is wide open in the out-of-plane direction, which means that the resolution δ_{q_y} in this direction is rather coarse [integration over q_y in Eq. (3); see also Refs. 16 and 27].

B. Scattering geometry

Figure 2 shows the paths of the various scans in reciprocal space. The momentum transfer $\mathbf{q}=\mathbf{k}_f-\mathbf{k}_i=(q_x,0,q_z)^T$ is given by $q_x=k_i(\cos\alpha_f-\cos\alpha_i)\approx k_i/2(\alpha_i-\alpha_f)\Phi$ and $q_z=k_i(\sin\alpha_f+\sin\alpha_i)\approx k_i\Phi$ (see Fig. 3). Therefore a reflectivity ($\alpha_i=\alpha_f$) corresponds to

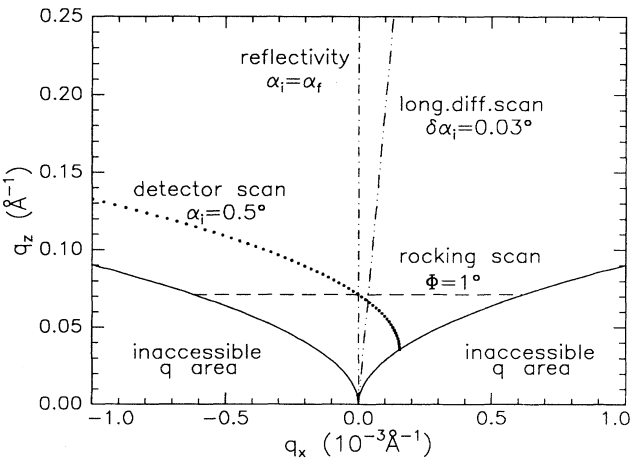

FIG. 2. Scans in reciprocal space (q_x,q_z). The region below the solid line is not accessible with the setup of this work. The dashed line is a rocking scan with a scattering angle $\Phi=\alpha_i+\alpha_f=1°$. The dash-dotted line represents a reflectivity ($\alpha_i=\alpha_f$, $q_x=0$) and the inclined dash-double-dotted line is a longitudinal diffuse scan with an offset $\delta\alpha_i=0.03°$. The path of a detector scan with incidence angle $\alpha_i=0.5°$ is given by the dotted line.

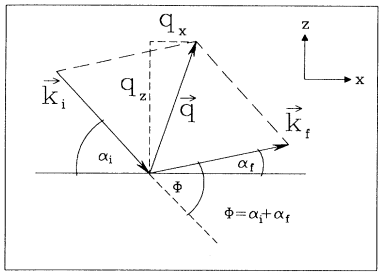

FIG. 3. Scattering geometry. The wave vectors of the incident and scattered x rays are $\mathbf{k}_i$ and $\mathbf{k}_f$, with the incidence and exit angles α_i and α_f, respectively, and the scattering angle Φ. The momentum transfer is defined by $\mathbf{q}=\mathbf{k}_f-\mathbf{k}_i=(q_x,q_z)^T$.

a q_z scan with $q_x=0$. A rocking scan is performed by rotating the sample at a fixed detector position. Thus the incidence angle α_i varies and the scattering angle $\Phi=\alpha_i+\alpha_f$ is constant. Rocking scans are nearly q_x scans at a fixed q_z position. By performing a detector scan, which means a scan with a fixed angle of incidence α_i and a varying scattering angle Φ, the q_x and the q_z component of the scattering vector are changed simultaneously. The path of this scan in reciprocal space is a parabola (see Fig. 3). A longitudinal diffuse scan is a nearly specular scan. The incidence angle α_i is slightly out of the specular condition, i.e., $\alpha_i-2\delta\alpha_i=\alpha_f$. In reciprocal space this scan lies on a straight line that is inclined at an angle $\delta\alpha_i$ against the q_z direction. All four different scan modes were performed during the measurements of the samples $S1-S3$. Due to geometric restrictions the marked area in Fig. 2 is not accessible with the experimental setup given in Sec. IV A.

V. MEASUREMENTS, RESULTS, AND DISCUSSION

A. Data analysis

A procedure that is widely used to fit x-ray reflectivities is the application of the model presented in Sec. II A after subtracting an off-specular longitudinal diffuse scan from the measurement to obtain the true specular data.[16] The resultant reflectivity is taken to yield the average density profile of the sample (layer thicknesses and rms roughnesses). But this method fails if the diffuse scattering peaks sharply at the specular condition.[46–48] Therefore, the data presented in this paper were *not* analyzed in this way: We measure a reflectivity, i.e., the whole intensity for $\alpha_i=\alpha_f$, and the diffuse scattering by performing several rocking curves, detector, and longitudinal diffuse scans. Afterward all data sets, the reflectivity and the off-specular scans, are fitted simultaneously. The amount of diffuse intensity in the specular direction is automatically calculated with the same parameters that are used for fitting the off-specular scans. In particular, the calculated reflectivity now is obtained by adding up the fitted diffuse intensity for $q_x=0$, calculated with Eq. (3), and the true specular intensity calculated with the model of Sec. II A. There are two major advantages of this method. First it is able to deal with diffuse scattering which contains a sharp peak at the specular ridge. Second is the fact that it yields one consistent set of model parameters for explaining both the diffuse as well as the true specular data. In other words, in our analysis the reflectivity is only one curve in a data set consisting of more than ten scans that are fitted simultaneously. A significant improvement of the fits of the diffuse scans may yield a fit of the reflectivity, which has a larger χ^2 than the best fit of the single true specular curve. However, there is no reason for neglecting the diffuse scattering data. In this work it is shown that completely different roughness values might be obtained if the diffuse scattering data are not taken into account (see Sec. V C).

Due to the fact that no absolute intensities were measured, two normalization factors were introduced: one for the diffuse intensity and one for the (true) specular intensity. The ratio between diffuse and specular intensity is directly obtained from the measurements and *not* a free fit parameter.

Furthermore, resolution effects as well as geometric correction factors were taken into account.[49,50] To obtain estimates for the error bars, the fit parameters were changed manually until a significant deviation between measurement and calculation occurs.

B. Measurements and fit results

Figures 4–6 show the measurements (open symbols) and the fits (solid lines) for sample $S1$. The data set consists of a reflectivity and a longitudinal diffuse scan with $\delta\alpha_i=0.10°$ (Fig. 4), two detector scans with $\alpha_i=0.20°$ and 0.40°, respectively (Fig. 5), and nine rocking curves in the region $0.057\le q_z\le 0.126$ Å^{-1} (Fig. 6). The simultaneous fit of the data yields the parameters given in the first column of Table II. It turns out that an inclusion of oxide layers improves the quality of the fits significantly. Therefore a three-layer model $SiO_2/Ge/GeO_2$ was assumed.

The oscillations due to the thickness of the Ge layer ($d_{Ge}=402$ Å) in the reflectivity and the longitudinal

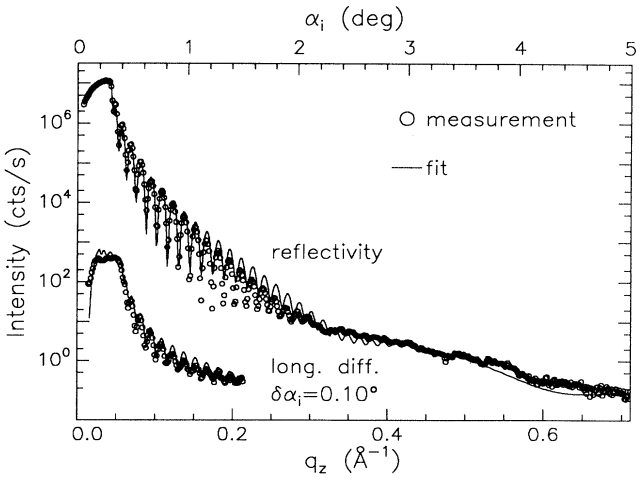

FIG. 4. Reflectivity and a longitudinal diffuse ($\delta\alpha_i=0.10°$) scan for sample $S1$. The measurements are represented by the dots and the fits are given by the solid lines.

diffuse scan in Fig. 4 are well reproduced by the fit. For intensity reasons the measurement of the longitudinal diffuse scan was limited to $q_z = 0.2$ Å^{-1}. The detector scans shown in Fig. 5 are also well explained by the model calculations. Note that the incidence angle $\alpha_i = 0.20°$ is below the critical angle $\alpha_{c,\mathrm{Ge}} = 0.29°$ of Ge. The resultant small penetration depth of the x rays leads only to scattering from the Ge/GeO_2 and GeO_2/air interfaces. In contrast to this behavior, the detector scan in the inset for $\alpha_i = 0.40° > \alpha_{c,\mathrm{Ge}}$ shows distinct modulations that are caused by strong correlations of the SiO_2/Ge and Ge/GeO_2 interfaces (see $\xi_\perp$ in Table II, which is larger than the thickness of the Ge layer). The peak in the diffuse scattering at $\alpha_f \approx \alpha_{c,\mathrm{Ge}}$ is the Yoneda peak. Although differences between the measurement and the fit in the region of the specular reflected beam are visible, one can say that the theory is able to explain these two different cases very well. The same statement holds for the rocking curves which are shown in Fig. 6. All locations and shapes of the dynamic peaks, which stem from interferences of the diffuse scattering from different interfaces and also contain information about the thicknesses and dispersions of the layers, are well reproduced by the fits using the theory of Holý and Baumbach.[23] The parameters are given in the first column of Table II.

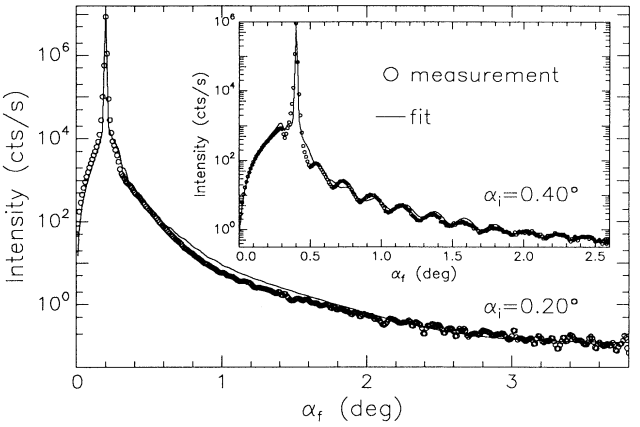

FIG. 5. Detector scans for sample *S*1. The incidence angles $\alpha_i = 0.20°$ and 0.40° (inset) were chosen. The solid lines are the results of the best fits and the symbols are the measurements.

The measurements (open symbols) and the fits (solid lines) for sample *S*2 are shown in Figs. 7–9. This data set consists of a reflectivity and a longitudinal diffuse scan with $\delta\alpha_i = 0.03°$ (Fig. 7), three detector scans for $\alpha_i = 0.15°$, 0.28°, and 0.50° (Fig. 8), and six rocking curves in the region $0.071 \le q_z \le 0.142$ Å^{-1} (Fig. 9). The simul-

TABLE II. Results of the simultaneous fits of the reflectivity and diffuse scattering data for the samples *S*1–*S*3. The values in parentheses were not varied in the fits and the parameters of the Si substrates are set to the theoretical numbers.

Layer		Sample *S*1	Sample *S*2	Sample *S*3
SiO_2				
	d (Å)	19±3	16.5±2.0	18.6±2.0
	$\delta\times10^6$	7.0±0.2	7.0±0.2	7.0±0.2
	σ (Å)	3.3±1.0	3.3±1.0	2.8±0.5
	ξ (Å)	300±200	700±300	1000±800
	h	(0.5)	0.4±0.2	(0.5)
Ge				
	d (Å)	402±3	392±2	490±3
	$\delta\times10^6$	13.0±0.2	13.3±0.2	13.7±0.2
	σ (Å)	32±5	12±3	8.6±2.0
	ξ (Å)	30 000±20 000	400±300	650±300
	h	0.23±0.1	0.15±0.05	0.4±0.1
Si				
	d (Å)		296±3	333±3
	$\delta\times10^6$		6.2±1.0	6.3±0.2
	σ (Å)		14±3	11±2
	ξ (Å)		10 000±5000	10 000±5000
	h		0.15±0.05	0.15±0.05
Ge				
	d (Å)			193±3
	$\delta\times10^6$			12.9±0.2
	σ (Å)			24±4
	ξ (Å)			20 000±10 000
	h			0.15±0.05
GeO_2				
	d (Å)	8±3		9±3
	$\delta\times10^6$	10.2±1.0		8.4±1.5
	σ (Å)	8.9±1.5		8.1±1.5
	ξ (Å)	≤100		900±400
	h	0.22±0.05		0.9±0.1
	$\xi_\perp$ (Å)	700±300	800±200	270±100

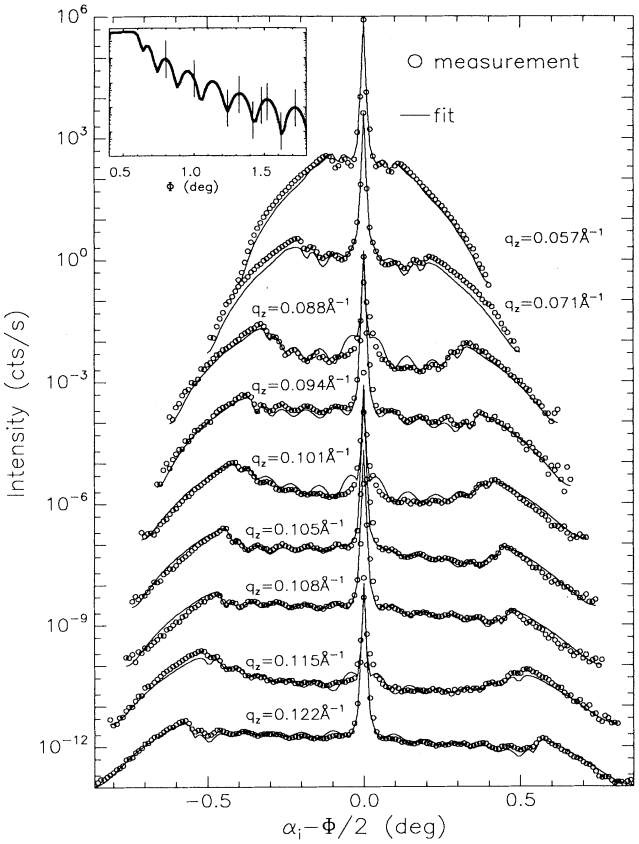

FIG. 6. Rocking curves for sample *S*1 in the region $0.80° \leq \Phi \leq 1.72°$. The symbols are the measurements and the solid lines represent the results of the simultaneous fit of the whole data set. The inset shows the first part of the reflectivity. For clarity the Φ positions of the transverse rocking scans are marked by vertical lines.

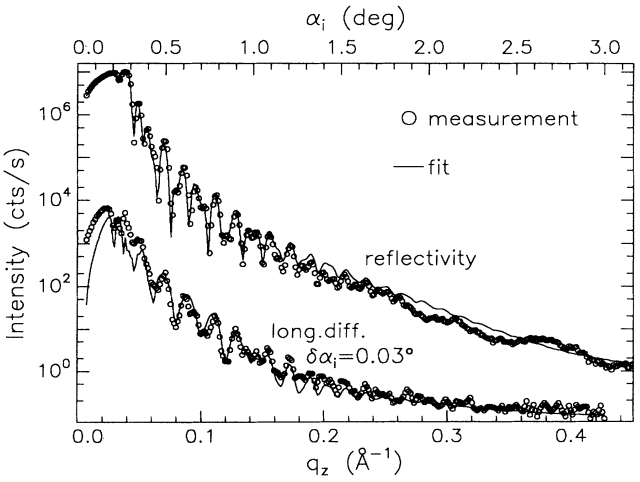

FIG. 7. Reflectivity and a longitudinal diffuse ($\delta\alpha_i = 0.03°$) scan for sample *S*2. The measurements are represented by the dots and the fits are given by the solid lines.

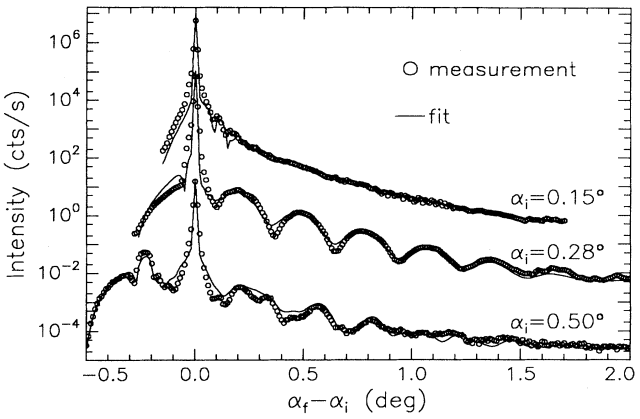

FIG. 8. Detector scans for sample *S*2. The incidence angles $\alpha_i = 0.15°$, 0.28°, and 0.50° were chosen. The solid lines are the results of the best fits and the symbols represent the measurements.

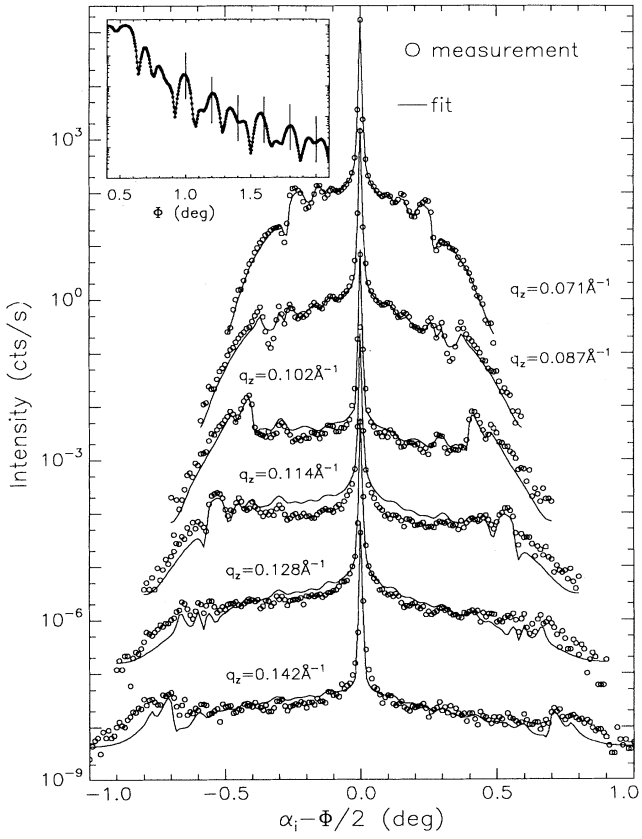

FIG. 9. Rocking curves for sample *S*2 in the region $1.00° \leq \Phi \leq 2.00°$. The symbols are the measurements and the solid lines represent the results of the simultaneous fit of the whole data set. The inset shows the first part of the reflectivity. For clarity the Φ positions of the transverse rocking scans are marked by vertical lines.

taneous fit of the data set leads to the parameters in the second column of Table II. In contrast to the sample *S*1, an inclusion of an oxide layer on top of the system does not improve the quality of the fits significantly. Therefore, again a three-layer model SiO_2/Ge/Si was assumed for this sample.

The reflectivity and the longitudinal diffuse scan now show a more complex structure (Fig. 7). Due to the different layer thicknesses ($d_{Ge}=392$ Å and $d_{Si}=296$ Å) a beating of the oscillations can be observed. Furthermore, two critical angles, one for the Si layer at $\alpha_{c,Si}=0.22°$ and one for the Ge layer at $\alpha_{c,Ge}=0.29°$, can be seen for very small incidence angles. The fit of the longitudinal diffuse scan is rather poor for small-q_z values. The amount of scattering for small angles cannot be reproduced by the fit. Possibly there was a small misalignment of the setup and remnants of the primary beam hit directly the detector.

The detector scans are shown in Fig. 8. They are well explained by the model calculations. Again different scattering depths were selected by choosing particular incidence angles. As the angle $\alpha_i=0.15°$ is smaller than the critical angle $\alpha_{c,Si}=0.22°$ of Si, the penetration depth of the x rays is very small and the scattering mainly stems from the topmost Si/air interface. The detector scan at an angle $\alpha_i=0.28°$, which is between $\alpha_{c,Si}$ and $\alpha_{c,Ge}$, shows modulations. They are caused by strong correlations of the Ge/Si and Si/air interfaces (see $\xi_\perp$ in Table II, which is more than twice as large as the thicknesses of the layers). But due to the limited penetration depth mainly the Si layer is seen by the x rays. If the incidence angle becomes larger, both layers contribute to the scattering and again a beating due to the different layer thicknesses is observed. This can be seen in the lower curve of Fig. 8, where for small exit angles α_f two Yoneda peaks with a particular shape can be seen. Although small deviations between the measurement and the fits close to the specular reflected beam are visible, the theory is able to explain all scans satisfactorily. The same statement holds for the rocking curves, which are shown in Fig. 9. The particular shape of these curves contains, like the reflectivity, detailed information about the layer thicknesses and dispersions. Furthermore, it turns out that they are less sensitive to the PSD's of the interfaces than the detector and longitudinal diffuse scans. Deviations between the measurements and the fits occur for larger scattering angles. In the regions of small incidence and exit angles, respectively, the amount of diffuse scattering is larger than the calculated intensity. As before, the reason might be a small misalignment of the setup.

The measurements (open symbols) and fits (solid lines) for sample *S*3 are shown in Figs. 10–12. This data set consists of a reflectivity and a longitudinal diffuse scan with $\delta\alpha_i=0.03°$ (Fig. 10), three detector scans for $\alpha_i=0.20°$, 0.50°, and 0.60°, respectively (Fig. 11), and five rocking curves in the region $0.068\le q_z\le 0.114$ Å^{-1} (Fig. 12). The simultaneous fit of the data yields the parameters given in the third column of Table II. As before, an inclusion of oxide layers improves the quality of the fits significantly. Therefore, for sample *S*3, a five-layer model

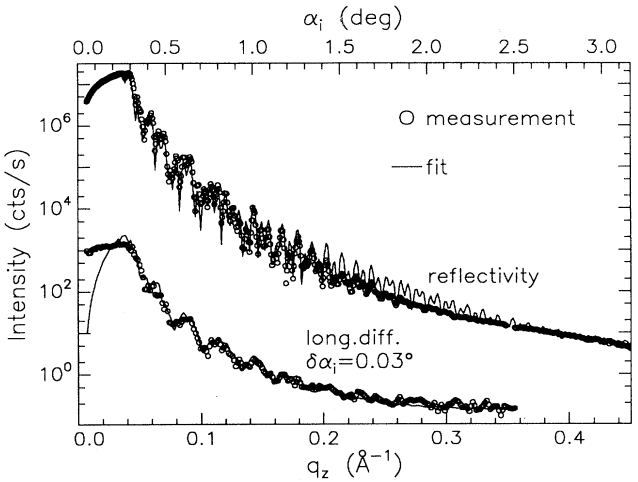

FIG. 10. Reflectivity and a longitudinal diffuse ($\delta\alpha_i=0.03°$) scan for sample *S*3. The measurements are represented by the dots and the fits are given by the solid lines.

SiO_2/Ge/Si/Ge/GeO_2 was assumed.

Due to interferences of the scattered waves from different layers of this sample, rather complex structures in the measured curves are observed. The oscillations stemming from the layer thicknesses ($d_{Ge,1}=490$ Å, $d_{Si}=333$ Å, and $d_{Ge,2}=193$ Å) in the reflectivity and the longitudinal diffuse scan in Fig. 10 are reproduced by the fit. The deviations of the measurement of the longitudinal diffuse scan and the respective fit for very small-q_z values may have the same sources as discussed for sample *S*2.

The agreement between the fits and the measurements of the three detector scans and the rocking curves in Figs. 11 and 12 is also rather good. The same incidence angles were chosen as for the samples *S*1 and *S*2 (different scattering depths). Again correlations between the layers have to be assumed to explain the observed modulations and all locations and shapes of the dynamic peaks that are sensitive to the PSD's of the interfaces were correctly

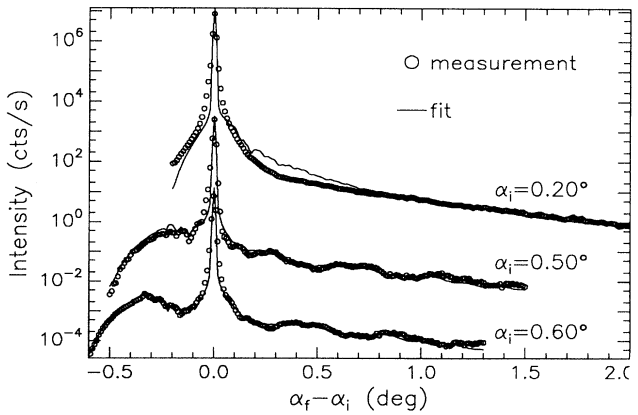

FIG. 11. Detector scans for sample *S*3. The incidence angles $\alpha_i=0.20°$, 0.50°, and 0.60° were chosen. The solid lines are the results of the best fits and the symbols represent the measurements.

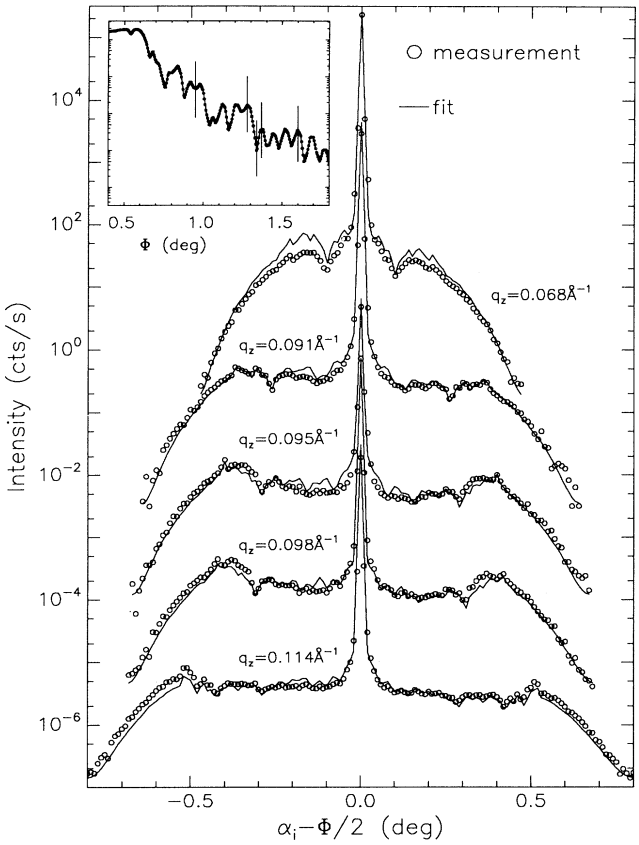

FIG. 12. Rocking curves for sample $S3$ in the region $0.95° \leq \Phi \leq 1.60°$. The symbols are the measurements and the solid lines represent the results of the simultaneous fit of the whole data set. The inset shows the first part of the reflectivity. For clarity the Φ positions of the transverse rocking scans are marked by vertical lines.

reproduced by the theory. The parameters of the fit of the whole data set are given in the last column of Table II.

C. Discussion

Table II shows the parameters that are obtained from the fits for each of the three samples $S1$–$S3$. For the Si substrates $\delta_{Si}=7.56\times10^{-6}$,[51] $\sigma_{Si}=1.0$ Å, $\xi_{Si}=20\,000$ Å, and $h_{Si}=0.5$ were assumed. The calculations are rather insensitive to variations of these parameters and therefore, instead of fit results, realistic values were used. The thicknesses, dispersions, and rms roughnesses of the SiO_2 layers can be determined with good accuracy. Within error they are equal for all three samples and the values are typical for thin native SiO_2 layers.[52] The lateral parameters of the SiO_2/Ge interfaces also can be determined from the calculations, but only with rather large errors. The Hurst parameters h of this interface were fixed at the value $h=0.5$ for samples $S1$ and $S3$.

The thicknesses of the evaporated layers are 12–40 % larger than the nominal values given in Sec. III. The reason for this is the aforementioned inaccuracy of the determination during the preparation process of the samples with the frequency shift of the quartz thickness monitor. The fits of the x-ray data (reflectivity and diffuse scattering data as well) are extremely sensitive to the film thicknesses and very accurate numbers are obtained (errors of only 1%). Furthermore, the electron densities (proportional to the dispersions δ_j) reach only 80–95 % of the values for single crystals of Si or Ge, respectively [the theoretical value for Ge is $\delta_{Ge}=14.4\times10^{-6}$ (Ref. 51)]. This can be expected for evaporated Si and Ge layers.[44]

The roughnesses of the interfaces between the evaporated layers vary between $\sigma=8$ and 32 Å. They increase from the substrate to the topmost layer for samples $S2$ and $S3$. Although $S3$ consists of no more than three evaporated layers, this tendency can clearly be seen ($\sigma_{Ge,1}=8.6$ Å $\Longrightarrow\sigma_{Si}=11.0$ Å $\Longrightarrow\sigma_{Ge,2}=24.0$ Å). Growth models predict laws of the form $\sigma\sim D^{\beta}$ with the total thickness D of the evaporated material and a growth exponent β which is $\beta\approx0.25$ for vapor deposited films [the Kardar-Parisi-Zhang (KPZ) model; for details see Refs. 11 and 53]. Although our data set is much too small for determining precise β values, for $S2$ and $S3$ a value of $\beta\approx0.2$ can be estimated if the last layer of $S3$ is excluded. Due to the GeO_2 on top, this layer shows a quite different behavior. Compared with sample $S1$ it turns out that the GeO_2 layers are very similar: They have rather small lateral correlation lengths ξ, roughnesses $\sigma=8$ Å, and thicknesses $d=9$ Å. The underlying Ge layers on top of the samples $S1$ and $S3$ show rather large roughnesses $\sigma=32$ and 24 Å, respectively. Therefore it is possible that the thin GeO_2 layers are not uniform. This is supported by the small correlation length, which indicates an island formation.

The correlation lengths of the interfaces between the evaporated layers are in the interval $500\leq\xi\leq20\,000$ Å. They increase from the substrate to the topmost layer for sample $S3$ too ($\xi_{Ge,1}=650$ Å $\Longrightarrow\xi_{Si}=10\,000$ Å $\Longrightarrow\xi_{Ge,2}=20\,000$ Å). Again growth models predict laws of the form $\xi\sim D^{1/z_s}$ with an exponent z_s, which, within the KPZ model, is $z_s=h/\beta\approx\frac{0.33}{0.25}$.[11,53] We can exclude this value for samples $S2$ and $S3$ because rather large ($\xi\geq10\,000$ Å) correlation lengths for the evaporated layers are obtained. But it must be mentioned that our systems are not well suited for a detailed study of this topic because only a small number of layers are present.

The obtained values for the Hurst parameter h of the interfaces of the evaporated layers are between 0.15 and 0.40. As can be seen from Fig. 1, interfaces with small h are very jagged. The magnitude of the parameter $\xi_\perp$ is of the order of the layer thicknesses for all samples. Therefore strong correlations between the interface roughnesses of the different layers are present for all samples. The rocking curves (see Figs. 6, 9, and 12), which are measured at scattering angles where a maximum of the reflected intensity was observed, show more diffusely scattered intensity than scans through the minima. This is an additional hint of strong correlations between the roughnesses of the interfaces even for small spatial frequencies[8] and confirms the rather large-$\xi_\perp$ values.

Obviously the scattering theory of Holý and Baum-

bach[23] combined with the simultaneous fit of all measurements is able to explain the data with only one consistent set of system parameters, which explains both the specularly reflected and the diffuse intensities. In this procedure the reflectivity is not a particular curve from which the layer thicknesses, dispersions, and rms roughnesses of the interfaces are determined. The diffuse scattering data are fully incorporated into the analysis and also have a strong influence on the obtained values for these parameters. This is of decisive importance, because for all samples which are investigated in this work, perfect fits of the (true) specular reflectivity can be obtained if the diffuse scattering data are neglected. For sample $S1$ a rms roughness of $\sigma = 8$ Å for the Ge/GeO_2 interface is the result of such a perfect fit, which differs strongly from the value $\sigma = 32$ Å as obtained by the simultaneous analysis of the whole data set (see Table II and Sec. V B). A value of $\sigma = 8$ Å for the Ge/GeO_2 interface is not able to explain the amount of diffuse scattering for sample $S1$. To confirm our results atomic force microscopy (AFM) measurements at different places on the surface of $S1$ were done. These measurements yield values between $\sigma_{AFM} = 22$ and 42 Å, which clearly means that a value of $\sigma = 8$ Å can be excluded. Other parameters, such as layer thicknesses and dispersions, that are obtained from the single fits of the true specular data differ only slightly from the values obtained from the fits that take the diffuse scattering data into account.

VI. SUMMARY, CONCLUSIONS, AND OUTLOOK

In summary, we have shown that for systems with a small number of layers (≤ 5) the DWBA is able to explain all features of the diffuse scattering data. Locations and shapes of diffuse peaks as well as different oscillation periods in the nonspecular scans were correctly described and the interface parameters (roughnesses, correlation lengths within the interfaces and between different layers, and Hurst parameters) can be quantitatively determined by fits using the theory of Holý and Baumbach.[23] Therefore the investigations of this work indicate that the DWBA gives a complete picture of the scattering of x rays in the region of total external reflection.

Furthermore, it is shown that the data sets have to be fitted simultaneously, which means that the reflectivity *and* the off-specular data have to be treated as one data set. A fit of this data set leads to one consistent set of system parameters that is able to explain all scans. If only the true specular data are analyzed a perfect fit might be the result, but unreliable values for the rms roughness may be obtained. This was shown for one sample and AFM measurements of the surface roughness confirm the values obtained from the presented fitting technique.

In future work some points concerning the DWBA have to be clarified. First, the condition $|q_z\sigma|^2 \leq 1$, which is often given as the range of validity of the DWBA, has to be proved experimentally. The measurements and the calculations of the present work may indicate that this range is much larger. Higher-order effects, as analyzed by de Boer,[19,20] may also be of particular importance for the data analysis in some special cases. Another important point is that it is not quite clear if the obtained rms roughnesses are the same for all scans. Because of different q_z ranges, the scans are sensitive to different spatial ranges of frequencies of the roughness spectrum. In particular cases this may lead to a rather large dependence of the rms roughnesses from q_z. Further investigations have to be done to clarify these points.

ACKNOWLEDGMENTS

We thank V. Nitz for the help during the experiments and H. Goebel (KfK Karlsruhe) for the AFM measurements.

*Present address: Manuel Lujan, Jr., Neutron Scattering Center, Los Alamos National Laboratory, Los Alamos, NM 87545.

†Present address: Mineralogisch-Petrographisches Institut, Grindelallee 48, 20146 Hamburg, Germany.

[1] H. Dosch, in *Critical Phenomena at Surfaces and Interfaces (Evanescent X-Ray and Neutron Scattering)*, edited by G. Höhler, Springer Tracts in Modern Physics Vol. 126 (Springer-Verlag, Berlin, 1992).

[2] R. W. James, *The Optical Principles of the Diffraction of X-Rays* (Ox Bow, Woodbridge, 1982).

[3] L. G. Parrat, Phys. Rev. **95**, 359 (1954).

[4] A. Abelés, Ann. Phys. (Paris) **5**, 596 (1950).

[5] J. Lekner, *Theory of Reflection* (Nijhoff, Dordrecht, 1987).

[6] J. Lekner, Physica B **173**, 99 (1991).

[7] L. B. Lurio, T. A. Rabedeau, P. S. Pershan, I. F. Silvera, M. Deutsch, S. D. Kosowsky, and B. M. Ocko, Phys. Rev. Lett. **68**, 2628 (1992).

[8] E. E. Fullerton, J. Pearson, C. H. Sowers, S. D. Bader, X. Z. Wu, and S. K. Sinha, Phys. Rev. B **48**, 17 432 (1993).

[9] M. K. Sanyal, S. K. Sinha, A. Gibaud, S. K. Satija, C. F. Majkrzak, and H. Homma, in *Surface X-Ray and Neutron Scattering*, edited by H. Zabel and I. K. Robinson, Springer Proceedings in Physics Vol. 61 (Springer-Verlag, Berlin, 1992), pp. 91–94.

[10] S. K. Sinha, M. K. Sanyal, S. K. Satija, C. F. Majkrzak, D. A. Neumann, H. Homma, S. Szpala, A. Gibaud, and H. Morkoc, Physica B **198**, 72 (1994).

[11] C. Thompson, G. Palasantzas, Y. P. Feng, S. K. Sinha, and J. Krim, Phys. Rev. B **49**, 4902 (1994).

[12] D. E. Savage, N. Schimke, Y.-H. Phang, and M. G. Lagally, J. Appl. Phys. **71**, 3283 (1992).

[13] Y.-H. Phang, R. Kariotis, D. E. Savage, and M. G. Lagally, J. Appl. Phys. **72**, 4627 (1992).

[14] D. E. Savage, Y.-H. Phang, J. J. Rownd, J. F. MacKay, and M. G. Lagally, J. Appl. Phys. **74**, 6158 (1993).

[15] M. R. Fitzsimmons and E. Burkel, Phys. Rev. B **47**, 8436 (1993).

[16] S. K. Sinha, E. B. Sirota, S. Garoff, and H. B. Stanley, Phys. Rev. B **38**, 2297 (1988).

[17] G. H. Vineyard, Phys. Rev. B **26**, 4146 (1982).

[18] R. Pynn, Phys. Rev. B **45**, 602 (1992).

[19] D. K. G. de Boer, Phys. Rev. B **49**, 5817 (1994).

[20] D. K. G. de Boer, Phys. Rev. B (to be published).

[21]Note that the specular reflected intensity calculated with the first-order DWBA causes this problem. In the present paper the specularly reflected intensity is always calculated using the exact Parrat formalism [Eq. (1)]. Fortunately, it turns out that the first-order diffuse scattering cross section as obtained by Sinha *et al.* (Ref. 16) is correct up to second order (Refs. 19 and 20).

[22]V. Holý, J. Kuběna, I. Ohlídal, K. Lischka, and W. Plotz, Phys. Rev. B **47**, 15 896 (1993).

[23]V. Holý and T. Baumbach, Phys. Rev. B **49**, 10 668 (1994).

[24]A. V. Andreev, A. G. Michette, and A. Renwick, J. Mod. Opt. **35**, 1667 (1988).

[25]A. P. Payne and B. M. Clemens, Phys. Rev. B **47**, 2289 (1993).

[26]J. Daillant and O. Bélorgey, J. Chem. Phys. **97**, 5824 (1992).

[27]D. Bahr, W. Press, R. Jebasinski, and S. Mantl, Phys. Rev. B **47**, 4385 (1993).

[28]Y. Yoneda, Phys. Rev. **131**, 2010 (1963).

[29]M. Born and E. Wolf, *Principles of Optics,* 2nd ed. (Pergamon, Oxford, 1964).

[30]W. A. Hamilton and R. Pynn, Physica B **173**, 71 (1991).

[31]A. Messiah, *Quantenmechanik* (de Gruyter, Berlin, 1985), Band 2.

[32]Similar expressions were also derived by S. K. Sinha, J. Phys. III **4**, 1543 (1994); D. K. G. de Boer (unpublished).

[33]B. B. Mandelbrot, *The Fractal Geometry of Nature* (Freeman, New York, 1982).

[34]M. F. Barnsley, R. L. Devaney, B. B. Mandelbrot, H.-O. Peitgen, D. Saupe, and R. F. Voss, *The Science of Fractal Images* (Springer-Verlag, Berlin, 1988).

[35]H. O. Peitgen, H. Jürgens, and D. Saupe, *Bausteine des Chaos-Fraktale* (Springer-Verlag, Berlin, 1992).

[36]Although the correlation function given by Eq. (4) allows values $h_j > 1$, it can be shown that for this particular $C_j(R)$ with $h_j > 1$, no real surface exists.

[37]R. Chiarello, V. Panella, J. Krim, and C. Thompson, Phys. Rev. Lett. **67**, 3408 (1991).

[38]G. Palasantzas, Phys. Rev. B **48**, 14 472 (1993).

[39]G. Palasantzas, Phys. Rev. B **49**, 10 544 (1994).

[40]Note that this is only true for small-q_z values. For large-q_z values the Born approximation yields that the diffuse scattering cross section is *not* proportional to the PSD, but to the Fourier transform of $\{\exp[q_z^2 C(\mathbf{R})]-1\}/q_z^2$ (Ref. 16).

[41]H. Sirringhaus, C. Schwarz, and H. v. Känel (unpublished).

[42]Z. H. Ming, A. Krol, Y. L. Soo, Y. H. Kao, J. S. Park, and K. L. Wang, Phys. Rev. B **47**, 16 373 (1993).

[43]A correlation function $C_{jk}(R)$ between interfaces has to fulfill the additional conditions for all $\mathbf{R}$: $|C_{jk}(\mathbf{R})|^2 \le C_j(0)C_k(0)$ and $|C_{jk}(\mathbf{R})|^2 \le \frac{1}{2}[C_j(0)+C_k(0)]$ [see, e.g., J. S. Bendat and A. G. Piersol, *Random Data: Analysis and Measurement Procedures* (Wiley-Interscience, New York, 1971)]. The particular function given by Eq. (5) always fulfills these conditions.

[44]R. J. Temkin, G. A. N. Connell, and W. Paul, in *Amorphous and Liquid Semiconductors,* edited by J. Stuke and W. Brenig (Taylor & Francis, London, 1974).

[45]L. Brügemann, R. Bloch, W. Press, and M. Tolan, Acta Crystallogr. Sec. A **48**, 688 (1992).

[46]Numerical tests show that for small-h_j values ($h_j < 0.2$) and rather large correlation lengths ξ_j, the diffuse scattering shows a narrow peak at the specular condition (Refs. 16 and 18).

[47]J. Daillant and O. Bélorgey, J. Chem. Phys. **97**, 5837 (1992).

[48]O. H. Seeck, P. Müller-Buschbaum, M. Tolan, and W. Press (unpublished).

[49]A. Gibaud, G. Vignaud, and S. K. Sinha, Acta Crystallogr. Sec. A **49**, 642 (1993).

[50]The specularly reflected beam was fitted assuming a Lorenzian line shape (see also Ref. 49) and the calculated intensities were convoluted with the resolution of the diffractometer. In addition, corrections which takes into account the narrow slit in front of the detector and the small incidence angles were done.

[51]*International Tables for Crystallography,* edited by A. J. C. Wilson (Kluwer Academic, Dordrecht, 1992), Vol. C.

[52]L. Brügemann, R. Bloch, W. Press, and P. Gerlach, J. Phys. C **2**, 8869 (1990).

[53]M. Kardar, G. Parisi, and Y. Zhang, Phys. Rev. Lett. **56**, 889 (1986).